Designing Efficient Solar-Driven Hydrogen Evolution Photocathodes Using Semitransparent MoQ_xCl_y (Q = S, Se) Catalysts on Si Micropyramids

*Qi Ding, Jianyuan Zhai, Miguel Cabán-Acevedo, Melinda J. Shearer, Linsen Li, Hung-Chih Chang, Meng-Lin Tsai, Dewei Ma, Xingwang Zhang, Robert J. Hamers, Jr-Hau He, and Song Jin**

To meet the growing global demand for renewable energy, water splitting using photoelectrochemical (PEC) devices is a promising approach to store solar energy in the form of a sustainable energy carrier such as hydrogen.[1–4] Two components are essential in a water splitting PEC device to achieve efficient solar-to-chemical fuel production:[4,5] a semiconductor (light absorber) that absorbs solar light and a catalyst that enhances the reaction kinetics.[6] P-type Si has been widely employed in tandem PEC systems as the photocathode for hydrogen evolution reaction (HER) because of its earth abundance and suitable bandgap.[7–10] However, one challenge of utilizing p-type silicon for PEC-HER is its intrinsic low photovoltage, which is limited by the Si/liquid junction.[10] N^+p Si can boost the photovoltage by replacing the Si/liquid junction with a built-in p-n junction.[9,10] In cases where the band alignment is influenced by the catalyst, the built-in p-n junction could also remove the constraints placed on the catalysts used in this system.[10] Studies have further shown that adding an additional p^+ layer on the back of n^+p Si could facilitate majority carrier collection and lead to improved fill factor and device performance.[11]

Besides large photovoltage, high photocurrent is another prerequisite for highly efficient PEC devices. Both the light harvesting properties of absorber and the optical transparency of catalysts deposited on absorber have significant impacts on the photocurrent.[5,12,13] To improve the insufficient light trapping ability of planar Si, nano- and microstructuring of Si have been investigated.[9,14–16] However, higher density of surface states and faster recombination rates simultaneously observed with increased surface area in Si nano- and microwire-based photocathodes prevented significant gains in efficiency so far.[9,10,17,18] Alternatively, Si micropyramid (MP)-based solar cells have been shown to exhibit high efficiency because of the omnidirectional broadband light-trapping ability.[19] Since micropyramid structured Si surface is etched along the (111) direction with the least dangling bonds,[20,21] it has the lowest surface state density as compared to structures such as silicon nanowires, cones or tubes, making them uniquely suited for PEC-HER light absorbers. Herein, we specifically design Si MPs with a favorable built-in n^+pp^+ junction as novel light absorbers for PEC-HER photocathodes, combining both improved light-harvesting ability and favorable band bending to maximize the overall solar conversion efficiency.

Another important factor for designing efficient PEC-HER photocathodes is the optimization of the HER electrocatalysts. Despite the wide variety of earth-abundant HER catalysts that have recently been investigated to replace noble metals,[6,22–33] only a few of them have been integrated into PEC systems.[13,17,18,34–41] Many problems need to be addressed in integrated PEC systems, such as the semiconductor/catalyst chemical incompatibility and stability issues, synthesis and controllability difficulties, induced interfacial defect states and recombination sites, and inefficient charge transfer across interfaces. Currently, catalysts are primarily evaluated based on their electrocatalytic activity. However, optical transparency of catalysts also plays a crucial role in the overall PEC performance. Despite good electrocatalytic activity, most reported HER catalysts suffer from strong light absorption or high reflection, which consequently reduces the light reaching the absorbers and decreases the generated photocurrent.[5,12,13] Hence, in those cases, balancing high catalyst loading and good optical transparency becomes one of the most challenging tasks. In this regard, catalysts with good optical transparency would present particular advantages. Nevertheless, the optical properties of HER electrocatalysts have rarely been systematically investigated to demonstrate the significance of good transparency in enabling high current density and high performance.

Q. Ding, J. Zhai, Dr. M. Cabán-Acevedo, M. J. Shearer, L. Li, Prof. D. Ma, Prof. X. Zhang, Prof. R. J. Hamers, Prof. S. Jin
Department of Chemistry
University of Wisconsin–Madison
1101 University Avenue, Madison, WI 53706, USA
E-mail: jin@chem.wisc.edu

H.-C. Chang, M.-L. Tsai, Prof. J.-H. He
Division of Computer
Electrical and Mathematical Sciences and Engineering
King Abdullah University of Science and Technology
Thuwal 23955-6900, Saudi Arabia

Prof. D. Ma
Department of Applied Physics
Zhejiang University of Technology
Hangzhou, Zhejiang Province 30023, China

Prof. X. Zhang
Key Laboratory of Biomass Chemical Engineering of Ministry of Education
College of Chemical and Biological Engineering
Zhejiang University
Hangzhou, Zhejiang Province 310027, China

DOI: 10.1002/adma.201501884

In this work, we fabricate highly efficient PEC-HER photocathodes by integrating amorphous MoQ_xCl_y (Q = S, Se) catalysts with n^+pp^+ Si MP absorber. We have previously reported MoS_xCl_y, synthesized via a low temperature chemical vapor deposition (CVD) reaction, as a stand-alone HER electrocatalyst,[40] exhibiting catalytic performance similar to 1T-MoS_2.[24] Here, we successfully extend this CVD synthesis method to amorphous $MoSe_xCl_y$ and demonstrate its significant HER catalytic activity. Moreover, we systematically evaluate the catalytic activity and the optical properties of MoS_xCl_y and $MoSe_xCl_y$, integrate them with planar p-Si and n^+pp^+ Si MP absorbers to fabricate photocathodes, and elucidate how the PEC performance is impacted by the choice of catalysts and light absorbers. We find that MoS_xCl_y is not only a highly active electrocatalyst for HER, but also a wide bandgap semiconductor with very low light absorption in the visible and near-infrared (IR) range. By integrating the MoS_xCl_y catalyst with n^+pp^+ Si MPs, we achieve the highest photocurrent density ever reported for Si-based PEC-HER photocathodes using non-noble metal catalysts due to a concurrent improvement in electrocatalytic activity, optical transparency, and light-harvesting capability.

We first used a low temperature CVD method to synthesize amorphous ternary compounds MoS_xCl_y and $MoSe_xCl_y$ on graphite, fused silica, and Si substrates to evaluate their catalytic and optical properties (see the Experimental Section for details). Molybdenum chloride ($MoCl_5$) was used as the precursor to incorporate Cl into the synthesized amorphous catalyst films. The employed low reaction temperatures led to the formation of amorphous materials with high degree of structural disorder and more active sites. At low temperatures, we expect the reaction rate to be limited by kinetics, which allow Cl anions to remain in the final product due to the homogenous but partial conversion of $MoCl_5$ precursor. The structural characterization of amorphous MoS_xCl_y has been described previously,[40] here we focus the discussion on $MoSe_xCl_y$. Raman spectroscopy and X-ray diffraction (XRD) measurements confirmed that the as-synthesized $MoSe_xCl_y$ films are amorphous (**Figure 1**a inset and Figure S1, Supporting Information). Energy-dispersive X-ray spectroscopy (EDS) confirmed the presence of Cl in the $MoSe_xCl_y$ film (Figure 1a) and showed the stoichiometry of Mo:Se:Cl to be around 1:2.0:1.2. Scanning electron microscopy (SEM) images of amorphous MoQ_xCl_y in comparison with crystalline MoQ_2 samples grown on graphite substrates are shown in Figure S2, Supporting Information. X-ray photoelectron spectroscopy (XPS) and ultraviolet photoelectron spectroscopy (UPS) were utilized to understand the chemical and structural differences between amorphous MoQ_xCl_y and crystalline MoQ_2. No Cl was present in crystalline MoQ_2, while a significant amount of Cl was observed in amorphous MoQ_xCl_y (Figure S3, Supporting Information). The work functions of MoS_xCl_y and $MoSe_xCl_y$ were determined to be 5.2 and 4.8 eV, respectively (Figure S3a, Supporting Information), which are significantly higher than those of the crystalline MoS_2 (4.4 eV)[40] and $MoSe_2$

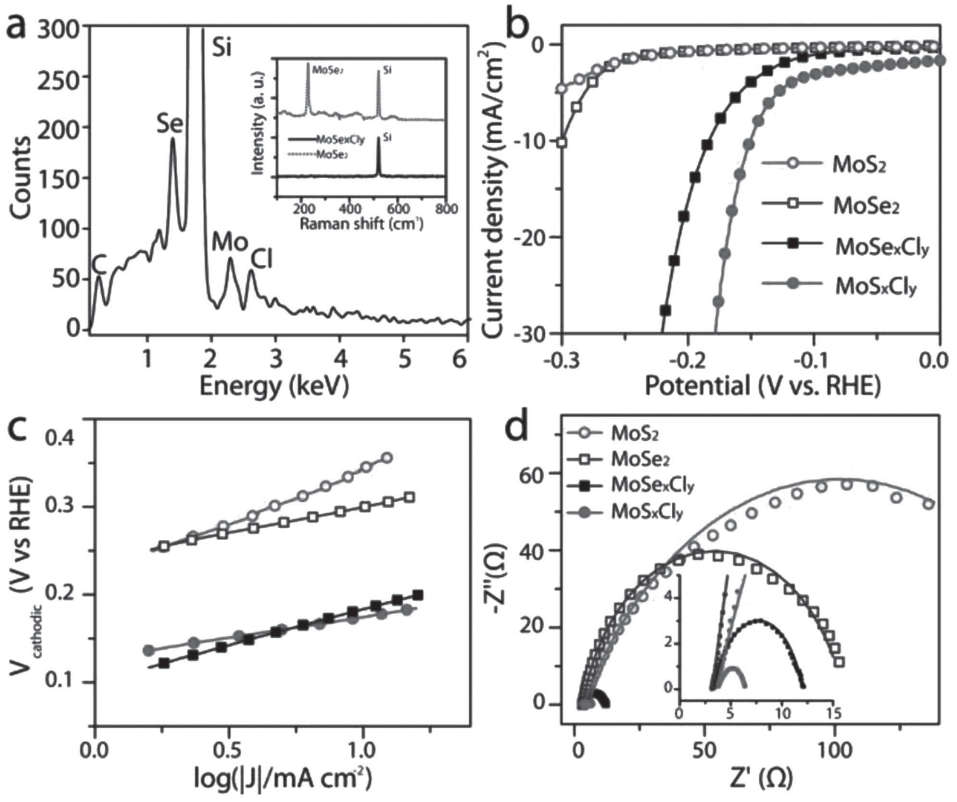

Figure 1. a) EDS and Raman (inset) of amorphous $MoSe_xCl_y$ deposited on Si substrate. Electrochemical characterization of amorphous MoS_xCl_y (solid circles) and $MoSe_xCl_y$ (solid squares) in comparison with crystalline MoS_2 (open circles) and $MoSe_2$ (open squares): b) Polarization curves, c) Tafel analysis, d) Nyquist impedance plots. The high frequency region of Nyquist impedance plots in (d) is magnified in the inset of (d).

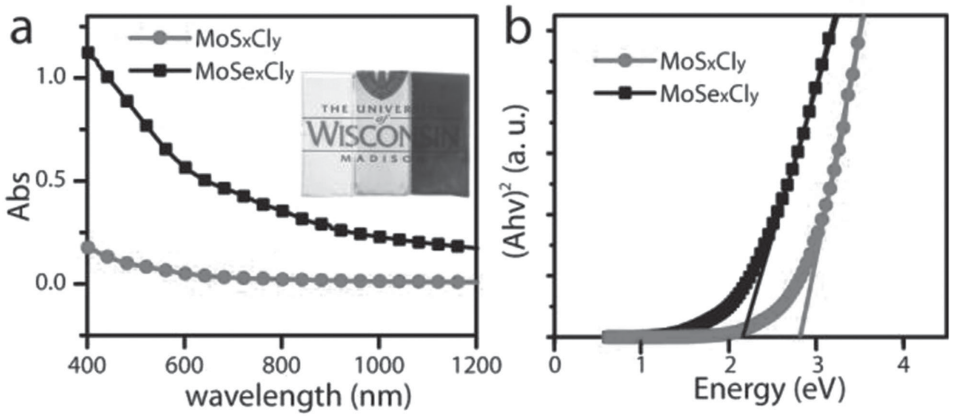

Figure 2. Optical characteristics of MoQ_xCl_y catalysts. a) Absorbance spectra of MoS_xCl_y (circles) and $MoSe_xCl_y$ (squares) grown on fused silica. Inset shows the digital images of bare fused silica (left), MoS_xCl_y on fused silica (middle) and $MoSe_xCl_y$ on fused silica (right). b) Tauc plots that allow the extraction of the optical gaps of MoS_xCl_y (circles) and $MoSe_xCl_y$ (squares) to be 2.8 and 2.2 eV, respectively.

(4.4 eV),[42] further highlighting the difference in properties between MoQ_xCl_y and MoQ_2.

The electrocatalytic activities of these amorphous MoQ_xCl_y compounds on graphite disks toward HER were then compared via standard rotating disk electrode (RDE) measurements in a three-electrode configuration in 0.5 M H_2SO_4 electrolyte (see the Experimental Section for details). Different CVD growth conditions were systematically investigated to optimize the new $MoSe_xCl_y$ electrocatalyst (Figure S4, Supporting Information). In general, lower reaction temperatures led to higher degree of structural disorders and higher concentration of active sites.[40] However, when the temperature was below 300 °C, the evaporation of precursors and deposition became limited, resulting in poor HER performance. The H_2 flow rate affected the catalytic performance of $MoSe_xCl_y$ (Figure S4, Supporting Information); therefore a small amount of H_2 flow was chosen for optimal $MoSe_xCl_y$ growth, but it did not affect the synthesis or performance of MoS_xCl_y. Figure 1b summarizes the polarization curves for the best performing MoS_xCl_y (grown at 275 °C) and $MoSe_xCl_y$ (grown at 400 °C) in comparison with crystalline MoS_2 and $MoSe_2$. As summarized in Table S1, Supporting Information, amorphous MoS_xCl_y and $MoSe_xCl_y$ exhibit catalytic onsets and significant H_2 evolution ($J_{cathodic} = -10$ mA cm^{-2}) at much lower overpotentials than crystalline MoQ_2, demonstrating a dramatic improvement in catalytic activity. We also observed significant differences in the Tafel slopes for MoQ_xCl_y and MQ_2, which reflects the differences in hydrogen adsorption energy and HER reaction mechanisms, which can be ultimately attributed to their electronic and structural differences. As shown in Figure 1c, MoS_xCl_y showed a Tafel slope of 48 mV decade^{-1}, suggesting a Volmer–Heyrovsky HER mechanism, in contrast to crystalline MoS_2, which showed Volmer–Tafel HER mechanism with a Tafel slope of 122 mV decade^{-1}. From $MoSe_2$ to $MoSe_xCl_y$, the Tafel slope changed from 60 to 82 mV decade^{-1}, suggesting a transition of the rate-determining step from electrochemical desorption to discharge. We also carried out electrochemical impedance spectroscopy (EIS) and fitted them using a simplified Randles equivalent circuit (Figure S5, Supporting Information) to investigate the electrode kinetics (Figure 1d). Amorphous MoS_xCl_y showed a smaller charge transfer resistance (R_{ct} = 2.7 Ω) than $MoSe_xCl_y$ (8.6 Ω), and both amorphous MoQ_xCl_y compounds exhibited an R_{ct} that was orders of magnitude smaller than crystalline MoS_2 (181 Ω) and $MoSe_2$ (101 Ω).

In addition to high electrocatalytic activity, high transparency with low optical losses is also highly desirable for an ideal catalyst in an integrated PEC system. To examine the optical properties with minimum interference from substrates, we purposely grew MoQ_xCl_y films on transparent fused silica substrates. The UV–Vis absorbance spectra of MoS_xCl_y and $MoSe_xCl_y$ (**Figure 2**a) clearly show that MoS_xCl_y has little absorption in the 500–1200 nm wavelength region, where Si most strongly absorbs solar light; whereas $MoSe_xCl_y$ shows much stronger absorption in this range. In fact, the difference between the two samples can be directly compared in their photographs (Figure 2a inset): MoS_xCl_y is highly transparent and hardly different from bare fused silica, whereas $MoSe_xCl_y$ exhibits a much darker color and less transparency. To better understand the origin of such difference, we used Tauc plots (Figure 2b) to estimate the optical bandgaps of MoS_xCl_y and $MoSe_xCl_y$ to be 2.8 and 2.2 eV, respectively. Both values are much larger than those of crystalline MoS_2 (1.3 eV) and $MoSe_2$ (1.1 eV).[43] The large optical gap of MoS_xCl_y is in agreement with its onset in the absorbance spectrum and well explains its low absorption in the visible and near-IR range. This suggests that MoQ_xCl_y, especially MoS_xCl_y, unlike most other electrocatalysts, will transmit the majority of the visible light important for solar energy harvesting. This rather unusual characteristic, combined with its high electrocatalytic activity, make MoS_xCl_y a unique and highly competitive catalyst material for PEC-HER.

Effective catalyst-semiconductor coupling is another key consideration for superior PEC performance. As demonstrated in our previous work,[41] direct CVD growth of a catalyst on Si provides higher quality interfaces with smaller charge transfer resistances, leading to much better PEC performance than samples made by dropcasting. Therefore, here we utilized low temperature CVD growth to directly integrate MoQ_xCl_y with Si to achieve high performance PEC devices. Simple p-type planar Si was first employed as the light absorber for a control experiment. A three-electrode configuration was used to measure

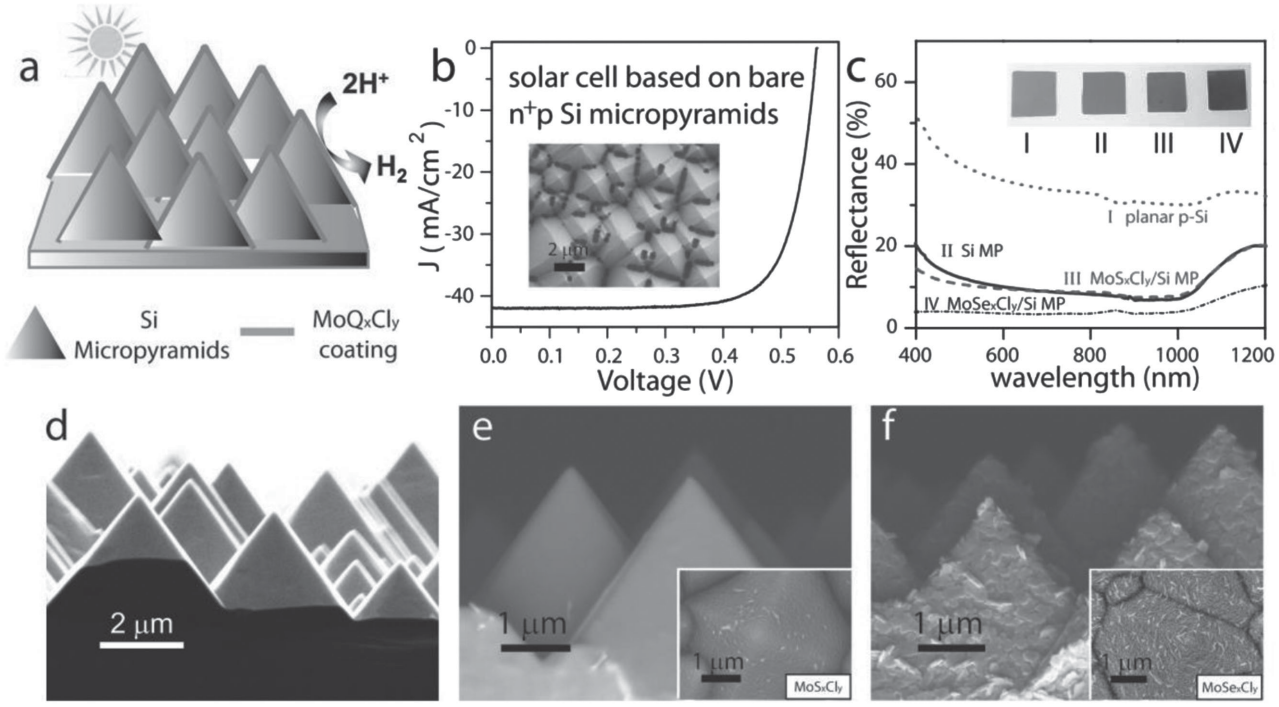

Figure 3. a) Schematic of MoQ_xCl_y catalysts coated on n^+pp^+ Si MPs for PEC hydrogen generation. b) *J–V* characteristics of a solar photovoltaic cell based on bare n^+pp^+ Si MPs. Inset shows a top-down SEM image of a bare Si MP substrate. c) Reflectance spectra of bare planar Si (I), Si MPs (II), MoS_xCl_y on Si MPs (III), and $MoSe_xCl_y$ on Si MPs (IV). Inset shows the corresponding photographs. Cross-sectional SEM images of d) bare Si MPs substrate, e) MoS_xCl_y/Si MPs and f) $MoSe_xCl_y$/Si MPs. Insets in (e, f) show the corresponding top-down SEM images of MoQ_xCl_y/Si.

the photocurrent density–potential (*J–E*) data in 0.5 M H_2SO_4 under simulated 1 Sun irradiation (see the Experimental Section for details). As shown in the *J–E* curves in Figure S6, Supporting Information, the onset potential (defined as the potential required to reach a photocurrent density of 0.5 mA cm^{-2}) shifted from –0.14 V versus reversible hydrogen potential (RHE) for bare planar p-Si to +0.27 V versus RHE for MoS_xCl_y/Si planar, and the photocurrent density at 0 V versus RHE increased from 0 to 20.6 mA cm^{-2}, which is comparable to a Pt/p-Si photocathode measured in the same condition.[38] The PEC performance of $MoSe_xCl_y$ on planar p-Si was also significantly improved compared to that of bare p-Si, but the improvement was not as much as with MoS_xCl_y. This difference could be attributed to multiple factors, including inferior HER catalytic activity, unfavorable band bending, not optimal growth conditions for $MoSe_xCl_y$, and potential presence of native silicon oxide at the interface.

The promising results achieved using simple planar p-Si photocathodes demonstrate the great potential of MoQ_xCl_y catalysts in PEC-HER. To further boost the performance and design more efficient PEC-HER systems, we utilized Si MPs with an n^+pp^+ junction as a more effective light absorber. The multiple scattering effect of MP structures allows more photons to enter the device hence significantly improves the omnidirectional light-harvesting ability[19] (**Figure 3**a). Moreover, the Si MPs could generate a much larger photovoltage owing to its built-in p-n junction. With the additional p^+ layer on the back of n^+p Si, the majority carrier collection could be further facilitated, reducing overall series resistance and improving the fill factor and device performance.[11] Figure 3b inset, d, shows the top-down and cross-sectional SEM images of the bare n^+pp^+ Si MP substrate. Prior to MoQ_xCl_y growth, a complete solid-state photovoltaic cell was fabricated to verify the solar performance of bare Si MPs. As shown in Figure 3b, a solar to electricity conversion efficiency of 17.6% was achieved with an open-circuit voltage (V_{oc}) of 0.56 V, a short-circuit current (J_{sc}) of 42.0 mA cm^{-2} and a fill factor (FF) of 0.75. Notably, the J_{sc} achieved here is much higher than what has been previously reported for planar Si solar cells, due to the improved light-harvesting ability of Si MPs. High V_{oc} and FF were also achieved, reflecting the large band bending and low charge recombination in the n^+pp^+ junction. After CVD growth, a conformal thin film of MoQ_xCl_y catalyst completely covered the Si MPs surface as illustrated in Figure 3a. MoS_xCl_y formed a smooth film with a thickness between 40 and 60 nm (Figure 3e and Figure S7, Supporting Information) and $MoSe_xCl_y$ also yielded a film around 40–60 nm but composed of dense nanoflakes and nanoparticles (Figure 3f and Figure S7, Supporting Information). The loading of MoS_xCl_y and $MoSe_xCl_y$ on Si micropyramid substrates were estimated using a microbalance to be roughly 10 and 12 μg cm^{-2}, respectively. UV–Vis spectra were measured to compare the reflectance between planar Si, Si MPs, and MoQ_xCl_y covered Si MPs. Much lower reflectance and higher absorption were recorded for Si MPs relative to planar p-Si (Figure 3c), which demonstrates the improved light-harvesting properties of Si MPs. Moreover, comparing MoS_xCl_y/Si MPs with bare Si MPs, we do not see significant change in their reflectance spectra, especially in the 500–1200 nm region where

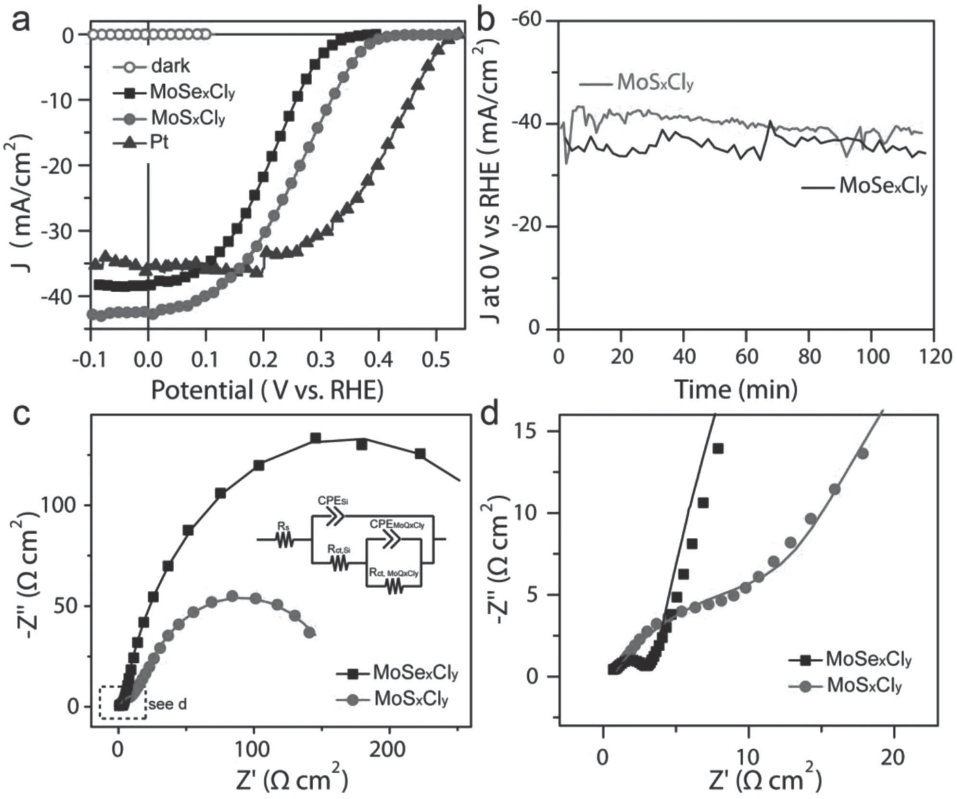

Figure 4. a) *J–E* curves for MoS_xCl_y/Si MPs (circles), $MoSe_xCl_y$/Si MPs (squares) and Pt/Si MPs (triangles) photocathodes measured in 0.5 M H_2SO_4 under simulated 1 Sun irradiation. b) Chronoamperometry measurement of MoQ_xCl_y/Si MPs photocathodes measured at 0 V versus RHE under illumination over 2 h. c) Nyquist impedance plots of MoS_xCl_y/Si MP (circles) and $MoSe_xCl_y$/Si MP (squares) measured under illumination. The dashed box in panel (c) is magnified in d). The solid line traces correspond to the fitting using the equivalent circuit in the inset of panel (c).

Si strongly absorbs solar light. This is attributed to the large bandgap and semitransparent nature of MoS_xCl_y catalyst film, and is consistent with the absorbance spectrum collected on MoS_xCl_y on fused silica (Figure 2a). In comparison, because of the larger absorbance of $MoSe_xCl_y$, a much darker color is seen in the photograph of $MoSe_xCl_y$ coated Si MPs (Figure 3c inset), which is also confirmed in the suppressed reflectance of $MoSe_xCl_y$/Si (Figure 3c).

To examine the advantage of n^+pp^+ Si MPs over planar p-Si and the influence of other parameters in PEC-HER systems, we fabricated different MoQ_xCl_y coated photocathodes and compared their PEC performance under simulated 1 Sun irradiation. The use of n^+pp^+ Si MPs results in a dramatic improvement in both the onset potential and photocurrent of the photocathodes. Specifically, as shown in **Figure 4**a and summarized in **Table 1**, the onset potential increased from 0.27 V versus RHE for MoS_xCl_y on planar p-Si to 0.41 V versus RHE for MoS_xCl_y on n^+pp^+ Si MPs, owing to the favorable band bending in the n^+pp^+ design. Similarly, the onset of $MoSe_xCl_y$ coated photocathodes also improved significantly from 0.18 V versus RHE to 0.35 V versus RHE. Moreover, the photocurrent density at 0 V versus RHE increased dramatically from 10–20 mA cm^{-2} for planar Si photocathodes to 35–43 mA cm^{-2} for Si MPs photocathodes, further demonstrating the effect of improved light harvesting by Si MPs. For comparison, Pt, the benchmark catalyst for HER, was also e-beam evaporated (5 nm) on Si MPs. Figure 4a highlights the difference among various catalysts and clearly shows the trend of decreasing onset potential with increasing HER overpotential. Pt/Si MP photocathode still exhibits the smallest catalytic overpotential and the highest onset potential at 0.53 V, closest to the V_{oc} of the Si MP solar cell. MoS_xCl_y shows better catalytic activity and smaller catalytic overpotential than $MoSe_xCl_y$, which results in the more positive onset potential for MoS_xCl_y on Si MPs in the PEC test. The difference in photocurrent density, on the other hand, is mostly caused by the difference in the optical transparency of the various catalysts. Even though Pt is the most active electrocatalyst, compared to MoS_xCl_y, Pt has less optical transparency, resulting in a smaller photocurrent density. Due to the large optical gap and minimum light absorption of

Table 1. Summary of *J* at 0 V versus RHE, onset potential and fill factor for various photocathodes: MoS_xCl_y on planar p-Si, MoS_xCl_y, $MoSe_xCl_y$, and Pt on n^+pp^+ Si MPs.

Photocathodes	*J* at 0 V versus RHE [mA cm^{-2}]	Onset potential [V]	Fill factor
MoS_xCl_y/Si planar	20.6	0.27	0.23
MoS_xCl_y/Si MPs	43.0	0.41	0.35
$MoSe_xCl_y$/Si MPs	38.8	0.35	0.34
Pt/Si MPs	36.7	0.53	0.47

MoS_xCl_y, the MoS_xCl_y/Si MP photocathode achieves a photocurrent density as high as 43 mA cm^{-2} at 0 V versus RHE, which is the highest current density ever reported for Si-based photocathodes and even surpasses that achieved by Pt/n^+pp^+ Si MPs. In addition, this high current density is close to the J_{sc} achieved for Si MP solar cells, suggesting minimal optical loss due to the catalyst coating, and is because of the synergistic effects of the efficient light-trapping property of the Si micropyramid structure and the high-transparency of the catalyst. To confirm the high photocurrent is indeed due to hydrogen generation, we used gas chromatography-mass spectrometer (GC-MS) to measure the amount of generated H_2 in comparison with the theoretical H_2 amount calculated from the measured photocurrent of the device integrated over time (Figure S8, Supporting Information). The Faradaic efficiency, which is defined as the experimental detected H_2 amount divided by the theoretical H_2 amount, is close to 100% for both MoS_xCl_y/Si MP and $MoSe_xCl_y$/Si MP photocathodes. As a result of the high current density and good photovoltage, excellent overall performance is achieved for all MoQ_xCl_y/n^+pp^+ Si MP photocathode systems (Table 1), with MoS_xCl_y/n^+pp^+ Si MPs representing one of the most efficient Si photocathode systems with non-noble metal catalysts.

Besides the high PEC performance, excellent stability is also demonstrated for these MoQ_xCl_y/Si MP photocathodes. Both MoS_xCl_y/Si MP and $MoSe_xCl_y$/Si MP photocathodes were tested under illumination at 0 V versus RHE for more than 2 h with negligible decreases in current density and PEC performance (Figure 4b). Compared with the 20% decrease in 1T-MoS_2/p-Si over the course of 2 h,[41] the stability of these MoQ_xCl_y/Si MPs has been greatly enhanced. This is due to the effective protection by the compact MoQ_xCl_y films conformally coated on the Si surface (Figure S7, Supporting Information). While other protective layers for Si have been reported, they could potentially block light absorption and lead to decreased photocurrent.[13,34] Therefore, the utilization of semitransparent catalysts like MoS_xCl_y to serve as both the catalytic and protective layer could enable high current density while maintaining good stability at the same time.

To provide more insights into the PEC performance, we conducted EIS measurements under illumination to elucidate the charge transfer resistances (R_{ct}) in MoQ_xCl_y/Si MP photocathodes. Two semicircles were observed in the Nyquist impedance plots for both photocathodes (Figure 4c,d), which were fitted using an equivalent circuit (Figure 4c inset) following reported examples of catalyst-semiconductor systems.[41,44] The charge transfer resistance across the absorber–catalyst interface ($R_{ct,\ Si}$) is a good indicator of the coupling between the light absorber and the catalyst. As reflected in the first semicircle, the $R_{ct,\ Si}$ is quite small for both MoS_xCl_y (18.6 Ω cm^2) and $MoSe_xCl_y$ (3.1 Ω cm^2), suggesting the benefits of the direct CVD growth in achieving high-quality interfaces between the absorber and catalyst. This fast charge transfer also lays the foundation for efficient utilization of electrons for hydrogen evolution, enabling better PEC performance. Moreover, the charge transfer resistance from the catalyst to the electrolyte ($R_{ct,}MoQ_xCl_y$), as depicted by the second semicircle, reflects the catalytic activity of the catalysts. MoS_xCl_y showed a smaller $R_{ct,}MoQ_xCl_y$ (155 Ω cm^2) compared to $MoSe_xCl_y$ (333 Ω cm^2), consistent with their electrocatalytic and photoelectrochemical performance shown in Figures 1 and 4a.

In summary, we have demonstrated that utilizing carefully designed Si micropyramids with an n^+pp^+ junction significantly improves both the photocurrent and photovoltage of photocathodes. More importantly, when such a semiconductor is integrated with a direct CVD grown MoS_xCl_y thin film, a catalyst that possesses both excellent HER catalytic activity and high optical transparency, we achieve the highest photocurrent density for Si-based PEC systems with non-noble metal catalysts with superior overall performance. Various design and optimization strategies regarding catalysts, absorbers, and coupling between the two have been systematically investigated to provide helpful guidelines on how to rationally design efficient photocathodes with optimal PEC performance.

Experimental Section

All chemicals were purchased from Sigma-Aldrich and used as received unless otherwise noted.

Fabrication of n^+pp^+ Si Micropyramids (MPs): Micropyramid arrays were fabricated on both sides of 150 μm thick p-type (100) Si wafers (dopant concentration of 5×10^{15} cm^{-3}) by chemical etching in a solution of potassium hydroxide (KOH, 45 vol%) and isopropyl alcohol (IPA). 300 nm of n^+ emitter layer (dopant concentration of 9×10^{19} cm^{-3}) was formed by thermal diffusion of $POCl_4$ at 1000 °C. 300 nm of p^+ back surface field layer (dopant concentration of 3×10^{20} cm^{-3}) was fabricated by screen printing Al and annealing at 500 °C.

Direct CVD Growth of MoQ_xCl_y onto Graphite, Fused Silica, and Si Substrates: Graphite disk substrates (6.0 mm diameter; <1 mm thick) were prepared by cutting and mechanically thinning slices of graphite rods (Ultra Carbon Corp., Ultra "F" Purity), followed by sequential sonication in acetone, isopropanol, ethanol and deionized water, and drying in an oven at 120 °C. Planar p-type Si wafers (B doped, resistivity of 1–2.5 Ω cm, (100) orientation, prime grade, 525 μm thickness, 100 mm diameter, native silicon oxide) were obtained from Silicon Inc. Graphite disk substrates were used for electrocatalytic activity measurement, and planar or micropyramid Si wafers were cut into small pieces for photocathode fabrication. Prior to growth on Si substrates, the native oxide layer on Si was removed via etching in aqueous buffered HF solution (Buffer HF Improved, Transene Inc.) for 15 s. The home-built CVD consists of a quartz tube (1 in. O.D.) connected with an Ar gas inlet and a vacuum pump, and equipped with pressure and gas flow controllers placed in a tube furnace (Lindberg/Blue M). The graphite disks and Si substrates were placed at the center of the tube furnace. Two alumina combustion boats containing 30–40 mg molybdenum (V) chloride ($MoCl_5$, 95%) and 500–700 mg elemental sulfur or selenium powders (99.5%), respectively, were initially placed outside of the tube furnace. Note $MoCl_5$ must be stored and weighed in a glovebox filled with inert gas, and when taken out of the glovebox must be sealed properly and quickly transferred into the CVD tube to avoid hydrolysis in air. The tube was evacuated to a base pressure of 10 mTorr and flushed three times with Ar carrier gas (99.999%) before the pressure was set to 780 Torr with Ar gas flowing at a rate of 125 sccm. For the synthesis of MoS_xCl_y, the furnace was heated to 225–375 °C with no H_2 gas flow, whereas for $MoSe_xCl_y$, the furnace was heated to 275–425 °C with 0–3 sccm H_2 flow. For making the best electrocatalysts and the best photocathodes, the optimal growth temperature for depositing MoS_xCl_y was 275 °C, and the optimal condition for depositing $MoSe_xCl_y$ was 400 °C with a 0.75 sccm H_2 gas flow. Once the temperature was stabilized, the two precursor boats were pushed into the mouth of the furnace (1.5 cm for $MoCl_5$ boat and 4.5 cm for S or Se boat) to initiate the reaction. The reaction was kept at the designated temperature for 10 min before the tube furnace was

opened to allow natural cooling to room temperature under Ar flow. The loading of MoS_xCl_y and $MoSe_xCl_y$ on Si micropyramid substrates were estimated using a microbalance to be roughly 10 and 12 μg cm^{-2}, respectively.

Structural Characterization: SEM was performed using a LEO Supra55 VP microscope operating at 3 kV. Raman spectra were taken using a Thermo Scientific DXR confocal Raman microscope using a 532 nm excitation laser. XPS was taken on a custom-built XPS system (Phi Electronics, Eden Prairie, MN), that included a model 10–610 Al K_α X-ray source (1486.6 eV photon energy) and a model 10–420 toroidal monochromator. A model 10–360 hemispherical analyzer with a 16-channel detector array was used, which under effective operating conditions had an analyzer resolution of 0.4 eV. Electrons were collected at an emission angle of 45° from the surface normal of the sample. High resolution data were collected for Mo3*d*, S2*p*, Se3*d*, O1*s*, and C1*s*. All XPS were shifted so that the adventitious carbon C1*s* peak was at 284.8 eV to make sure the data across samples were aligned and that the samples were not experiencing differential charging effects that might convolute the data. The same setup with an UV light source of a He I discharge lamp (21.2 eV photon energy) was utilized for UPS. Electrons were collected at a 0° take-off angle from the surface normal with analyzer resolution of 0.09 eV. The location of the Fermi level was determined using platinum by setting the valence band maximum of platinum to zero. All data reported contain a Fermi level that has been set to 0 eV.

Electrochemical Characterization of Catalytic Activity toward Hydrogen Evolution Reaction (HER): All electrochemical measurements were performed in a three-electrode configuration using a RDE setup (Bioanalytical Systems, Inc.; RDE-2) with a Bio-Logic SP-200 potentiostat. 0.5 M H_2SO_4 (aq) was used as the electrolyte and continuously purged with H_2(g) (99.999%). A saturated calomel reference electrode (SCE) (CH Instruments) was used as the reference electrode and a graphite rod (National Carbon Co., AGKSP Spectroscopic Electrode) was used as the counter electrode. The graphite disks covered with catalysts were affixed to a glassy carbon RDE tip using silver paint (Ted Pella, PELCO Colloidal Silver). The SCE was calibrated against the RHE using a platinum wire (Kurt J. Lesker, 99.99%; 0.50 mm diameter) as both the working and counter electrodes to allow potentials to be referenced against RHE. Linear sweep or cyclic voltammograms were measured from +0.25 V to −0.45 V versus RHE at a scan rate of 3 mV s^{-1} in both the forward and reverse directions at a rotating speed of 2000 rpm. After voltammetric characterization, EIS was performed at −0.24 V versus RHE, applying a sinusoidal voltage with an amplitude of 10 mV and scanning frequency from 200 kHz to 50 mHz. The EIS spectra were modeled using a simplified Randles equivalent circuit (Figure S5, Supporting Information), which consists of a resistor (R_s) in series with a parallel arrangement of a resistor (R_{ct}) and a constant phase element (CPE).

Fabrication of Photocathodes: Si photocathodes were fabricated following reported procedures.[1] Briefly, the back side of the Si substrates was first scratched with a diamond scribe, and then a coiled Cu wire was embedded in a Ga/In eutectic mixture (Aldrich) onto the scratched Si surface, forming an Ohmic back contact. Silver paint (Ted Pella) was then used to affix the Cu wire. After drying, the Cu lead was passed into a 2 mm diameter glass tube, and the Si electrode and Cu wire were then encased in Hysol 9460 epoxy. Calibrated digital images and ImageJ were used to determine the geometrical area of the exposed electrode surface defined by epoxy. Planar p-type Si photocathodes were etched in aqueous buffered HF solution (Buffer HF Improved, Transene Inc.) for 30 s and n^+pp^+ Si MPs photocathodes were etched for 1–5 s to remove the native silicon oxide on the surface prior to measurements.

Photoelectrochemical Characterization: The photoelectrochemical characteristics of MoQ_xCl_y/Si photocathodes were measured in a three-electrode configuration using a Bio-Logic SP-200 potentiostat under simulated 1 Sun irradiation (100 mW cm^{-2}) provided by a 1 kW Xe short arc lamp solar simulator (Newport Corp., Model 91191; AM1.5G filter). A Si photodiode (Thorlabs) was utilized to calibrate the light intensity by generating a photocurrent equal to that at 100 mW cm^{-2} light intensity. 0.5 M H_2SO_4 was used as the electrolyte, a graphite rod was used as the counter electrode, and a SCE was used as the reference electrode. The electrolyte was vigorously stirred to minimize mass transport limitations and remove accumulated hydrogen gas bubbles on the electrode surface, and constantly purged with research-grade H_2 gas (99.999%) to maintain a constant Nernst potential for H^+/H_2 redox couple. The current density versus potential (*J*–*E*) data were measured with a scan rate of 10 mV s^{-1}, and were not corrected for any uncompensated resistance losses or any other extrinsic losses. EIS was performed at a constant potential of +0.40 V versus RHE while sweeping the frequency from 350 kHz to 1 Hz with a 10 mV AC dither and modeled using the equivalent circuit shown in the inset of Figure 4c.

Hydrogen Measurement: The amount of generated H_2 was detected using gas chromatography-mass spectrometer (GC-MS). Both MoS_xCl_y/Si MP and $MoSe_xCl_y$/Si MP photocathodes were illuminated at 0 V versus RHE under simulated 1 Sun irradiation for more than 1 h with no H_2 bubbling. A syringe was used to periodically remove 500 μL from the headspace of a sealed cell, and then injected into a gas chromatography-mass spectrometer (GCMS-QP2010 Ultra, Shimadzu Scientific Instruments). The total amount of H_2 generated in the cell was then calculated based on the detected H_2 amount in the GCMS measurement. The total amount of charge Q(C) passed through the cell was calculated by integrating the measured current over time.

Supporting Information

Supporting Information is available from the Wiley Online Library or from the author.

Acknowledgements

This research was supported by the U.S. Department of Energy, Office of Basic Energy Sciences, Division of Materials Sciences and Engineering, under Award No. DE-FG02–09ER46664. S.J. also thanks UW–Madison H. I. Romnes Faculty Fellowship for support. M.C. thanks the NSF Graduate Research Fellowship for support. The authors thank Mr. Donghyeon Kang and Prof. Kyoung-Shin Choi for their assistance with the GC-MS measurements.

Received: April 20, 2015
Revised: July 8, 2015
Published online: September 21, 2015

[1] N. S. Lewis, D. G. Nocera, *Proc. Natl. Acad. Sci. USA* **2006**, *103*, 15729.
[2] J. A. Turner, *Science* **2004**, *305*, 972.
[3] D. G. Nocera, *Acc. Chem. Res.* **2012**, *45*, 767.
[4] M. G. Walter, E. L. Warren, J. R. McKone, S. W. Boettcher, Q. X. Mi, E. A. Santori, N. S. Lewis, *Chem. Rev.* **2010**, *110*, 6446.
[5] J. R. McKone, N. S. Lewis, H. B. Gray, *Chem. Mater.* **2014**, *26*, 407.
[6] M. S. Faber, S. Jin, *Energy Environ. Sci.* **2014**, *7*, 3519.
[7] K. Sun, S. H. Shen, Y. Q. Liang, P. E. Burrows, S. S. Mao, D. L. Wang, *Chem. Rev.* **2014**, *114*, 8662.
[8] S. Y. Reece, J. A. Hamel, K. Sung, T. D. Jarvi, A. J. Esswein, J. J. H. Pijpers, D. G. Nocera, *Science* **2011**, *334*, 645.
[9] S. W. Boettcher, J. M. Spurgeon, M. C. Putnam, E. L. Warren, D. B. Turner-Evans, M. D. Kelzenberg, J. R. Maiolo, H. A. Atwater, N. S. Lewis, *Science* **2010**, *327*, 185.
[10] S. W. Boettcher, E. L. Warren, M. C. Putnam, E. A. Santori, D. Turner-Evans, M. D. Kelzenberg, M. G. Walter, J. R. McKone, B. S. Brunschwig, H. A. Atwater, N. S. Lewis, *J. Am. Chem. Soc.* **2011**, *133*, 1216.

[11] D. Bae, T. Pedersen, B. Seger, M. Malizia, A. Kuznetsov, O. Hansen, I. Chorkendorff, P. C. K. Vesborg, *Energy Environ. Sci.* **2015**, *8*, 650.
[12] H. P. Wang, K. Sun, S. Y. Noh, A. Kargar, M. L. Tsai, M. Y. Huang, D. L. Wang, J. H. He, *Nano Lett.* **2015**, *15*, 2817.
[13] J. D. Benck, S. C. Lee, K. D. Fong, J. Kibsgaard, R. Sinclair, T. F. Jaramillo, *Adv. Energy Mater.* **2014**, *4*, 1400739.
[14] M. D. Kelzenberg, S. W. Boettcher, J. A. Petykiewicz, D. B. Turner-Evans, M. C. Putnam, E. L. Warren, J. M. Spurgeon, R. M. Briggs, N. S. Lewis, H. A. Atwater, *Nat. Mater.* **2010**, *9*, 368.
[15] B. M. Kayes, H. A. Atwater, N. S. Lewis, *J. Appl. Phys.* **2005**, *97*, 114302.
[16] S. Jeong, S. Wang, Y. Cui, *J. Vac. Sci. Technol. A* **2012**, *30*, 060801.
[17] J. R. McKone, E. L. Warren, M. J. Bierman, S. W. Boettcher, B. S. Brunschwig, N. S. Lewis, H. B. Gray, *Energy Environ. Sci.* **2011**, *4*, 3573.
[18] E. L. Warren, J. R. McKone, H. A. Atwater, H. B. Gray, N. S. Lewis, *Energy Environ. Sci.* **2012**, *5*, 9653.
[19] H. P. Wang, T. Y. Lin, C. W. Hsu, M. L. Tsai, C. H. Huang, W. R. Wei, M. Y. Huang, Y. J. Chien, P. C. Yang, C. W. Liu, L. J. Chou, J. H. He, *ACS Nano* **2013**, *7*, 9325.
[20] M. Edwards, S. Bowden, U. Das, M. Burrows, *Sol. Energy Mater. Sol. Cells* **2008**, *92*, 1373.
[21] U. Neuwald, H. E. Hessel, A. Feltz, U. Memmert, R. J. Behm, *Surf. Sci.* **1993**, *296*, L8.
[22] J. D. Benck, T. R. Hellstern, J. Kibsgaard, P. Chakthranont, T. F. Jaramillo, *ACS Catal.* **2014**, *4*, 3957.
[23] C. G. Morales-Guio, X. L. Hu, *Acc. Chem. Res.* **2014**, *47*, 2671.
[24] M. A. Lukowski, A. S. Daniel, F. Meng, A. Forticaux, L. S. Li, S. Jin, *J. Am. Chem. Soc.* **2013**, *135*, 10274.
[25] M. A. Lukowski, A. S. Daniel, C. R. English, F. Meng, A. Forticaux, R. J. Hamers, S. Jin, *Energy Environ. Sci.* **2014**, 2608.
[26] M. S. Faber, R. Dziedzic, M. A. Lukowski, N. S. Kaiser, Q. Ding, S. Jin, *J. Am. Chem. Soc.* **2014**, *136*, 10053.
[27] M. S. Faber, M. A. Lukowski, Q. Ding, N. S. Kaiser, S. Jin, *J. Phys. Chem. C* **2014**, *118*, 21347.
[28] D. S. Kong, H. T. Wang, Z. Y. Lu, Y. Cui, *J. Am. Chem. Soc.* **2014**, *136*, 4897.
[29] Q. Liu, J. Q. Tian, W. Cui, P. Jiang, N. Y. Cheng, A. M. Asiri, X. P. Sun, *Angew. Chem. Int. Ed.* **2014**, *53*, 6710.
[30] D. Merki, S. Fierro, H. Vrubel, X. L. Hu, *Chem. Sci.* **2011**, *2*, 1262.
[31] D. Voiry, H. Yamaguchi, J. W. Li, R. Silva, D. C. B. Alves, T. Fujita, M. W. Chen, T. Asefa, V. B. Shenoy, G. Eda, M. Chhowalla, *Nat. Mater.* **2013**, *12*, 850.
[32] E. J. Popczun, C. G. Read, C. W. Roske, N. S. Lewis, R. E. Schaak, *Angew. Chem. Int. Ed.* **2014**, *53*, 5427.
[33] E. J. Popczun, J. R. McKone, C. G. Read, A. J. Biacchi, A. M. Wiltrout, N. S. Lewis, R. E. Schaak, *J. Am. Chem. Soc.* **2013**, *135*, 9267.
[34] B. Seger, A. B. Laursen, P. C. K. Vesborg, T. Pedersen, O. Hansen, S. Dahl, I. Chorkendorff, *Angew. Chem. Int. Ed.* **2012**, *51*, 9128.
[35] C. G. Morales-Guio, S. D. Tilley, H. Vrubel, M. Gratzel, X. L. Hu, *Nat. Commun.* **2014**, *5*, 3059.
[36] Y. D. Hou, B. L. Abrams, P. C. K. Vesborg, M. E. Bjorketun, K. Herbst, L. Bech, A. M. Setti, C. D. Damsgaard, T. Pedersen, O. Hansen, J. Rossmeisl, S. Dahl, J. K. Norskov, I. Chorkendorff, *Nat. Mater.* **2011**, *10*, 434.
[37] S. P. Berglund, H. He, W. D. Chemelewski, H. Celio, A. Dolocan, C. B. Mullins, *J. Am. Chem. Soc.* **2014**, *136*, 1535.
[38] U. Sim, T. Y. Yang, J. Moon, J. An, J. Hwang, J. H. Seo, J. Lee, K. Y. Kim, J. Lee, S. Han, B. H. Hong, K. T. Nam, *Energy Environ. Sci.* **2013**, *6*, 3658.
[39] Y. J. Sun, C. Liu, D. C. Grauer, J. K. Yano, J. R. Long, P. D. Yang, C. J. Chang, *J. Am. Chem. Soc.* **2013**, *135*, 17699.
[40] X. Zhang, F. Meng, S. Mao, Q. Ding, M. J. Shearer, M. S. Faber, J. Chen, R. J. Hamers, S. Jin, *Energy Environ. Sci.* **2015**, *8*, 862.
[41] Q. Ding, F. Meng, C. R. English, M. Caban-Acevedo, M. J. Shearer, D. Liang, A. S. Daniel, R. J. Hamers, S. Jin, *J. Am. Chem. Soc.* **2014**, *136*, 8504.
[42] T. Shimada, F. S. Ohuchi, B. A. Parkinson, *Jpn. J. Appl. Phys., Part 1* **1994**, *33*, 2696.
[43] S. K. Mahatha, K. D. Patel, K. S. R. Menon, *J. Phys.: Condens. Matter* **2012**, *24*, 475504.
[44] B. Klahr, S. Gimenez, F. Fabregat-Santiago, J. Bisquert, T. W. Hamann, *J. Am. Chem. Soc.* **2012**, *134*, 16693.